

Thermal atomic layer etching mechanism of amorphous aluminum oxide by hydrogen fluoride and trimethylaluminum: First-principles study

Khabib Khumaini ^{a,b}, Gyejun Cho ^a, Hye-Lee Kim ^{a,c}, Won-Jun Lee ^{a,c,*}

^a Department of Nanotechnology and Advanced Materials Engineering, Sejong University, Seoul 05006, Republic of Korea

^b Department of Chemistry, Universitas Pertamina, Jakarta 12220, Indonesia

^c Metal-organic Compounds Materials Research Center, Sejong University, Seoul 05006, Republic of Korea

ARTICLE INFO

Keywords:

Atomic layer etching
Aluminum oxide
Density functional theory
Hydrogen fluoride
Trimethylaluminum
Aluminum fluoride

ABSTRACT

We present a first-principles density functional theory (DFT) study of the mechanism of thermal atomic layer etching (ALE) of aluminum oxide (Al_2O_3). Using amorphous Al_2O_3 and aluminum fluoride (AlF_3) slab models generated by ab initio molecular dynamics and optimized by DFT, we simulated the sequential surface reactions. The fluorination reactions with hydrogen fluoride (HF), leading to the formation of multilayer AlF_3 and the release of H_2O and CH_4 , were calculated to occur spontaneously at 250 °C with low activation energies ranging from 0.18 to 1.14 eV. The subsequent removal reactions with trimethylaluminum (TMA) were also spontaneous, with low activation energies of less than 1.08 eV, releasing the dimethylaluminum fluoride dimer. Our results indicate that the Al_2O_3 ALE is thermodynamically favorable and kinetically accessible at 250 °C, which agrees with experimental observations in the literature. In addition, the self-limiting nature of the removal step and the formation of multilayer AlF_3 were also explained.

1. Introduction

Atomic layer processing is becoming essential for the fabrication of advanced three-dimensional devices. Atomic Layer Deposition (ALD) is a well-established technique that uses sequential, self-limiting surface reactions to deposit thin films with excellent conformality and atomic-scale thickness control [1]. Complementary to ALD, atomic layer etching (ALE) uses sequential surface modification and removal steps, which can be partially or fully self-limiting, allowing material removal with atomic precision [2]. ALE is broadly categorized into plasma ALE and thermal ALE. Plasma ALE is inherently anisotropic because it relies on ion bombardment to remove the modified layer. In contrast, thermal ALE is isotropic because it uses chemical reactions to form and remove the modified layer.

Thermal ALE was first demonstrated for aluminum oxide (Al_2O_3) films using hydrogen fluoride (HF) for surface modification and tin(II) acetylacetone ($\text{Sn}(\text{acac})_2$) for removal reactions [3]. Subsequent studies have reported several ALE processes for Al_2O_3 using different combinations, including combinations of HF with trimethylaluminum ($\text{Al}(\text{CH}_3)_3$, TMA) [4], dimethylaluminum chloride ($\text{AlCl}(\text{CH}_3)_2$, DMAC) [5], or boron chloride (BCl_3) [6], as well as niobium(V) fluoride (NbF_5

with carbon tetrachloride (CCl_4) [7].

The surface reactions governing the thermal ALE of Al_2O_3 by HF and TMA have been investigated by *in situ* characterization. During HF exposure, the hydroxyl ($-\text{OH}$) and methyl ($-\text{CH}_3$) groups are replaced by fluorine atoms, which were detected by *in situ* Fourier transform infrared (FTIR) spectroscopy [4]. This resulted in the formation of the AlF_3 layer and the release of H_2O , which were detected by *in situ* X-ray photoelectron spectroscopy (XPS) [8] and quadrupole mass spectrometry (QMS) [9], respectively.

However, in contrast to ALD, a comprehensive atomic-level theoretical understanding of the thermal ALE process remains limited. The fluorination of bare theta-alumina by HF at 0 K has been simulated by density functional theory (DFT) calculations [10]. These calculations indicated that the fluorination reactions are exothermic but suggested that H_2O formation is unfavorable due to high activation energies above 1.63 eV. Critically, the activation energy of the fluorination reaction itself was not calculated, and the reaction of HF with $-\text{OH}$ or $-\text{CH}_3$ groups was not considered. More recently, a DFT study investigated the removal reaction of crystalline alpha- AlF_3 by TMA and showed it to be thermodynamically favorable [11]. Nevertheless, a calculated activation energy of 1.49 eV was reported, which is relatively high considering

* Corresponding author at: Department of Nanotechnology and Advanced Materials Engineering, Sejong University, 209 Neungdong-ro, Gwangjin-gu, Seoul 05006, Republic of Korea.

E-mail address: wjlee@sejong.ac.kr (W.-J. Lee).

typical ALE process temperatures of 150–325 °C [12].

In our previous work, we investigated the gas-phase etching mechanism of amorphous hydrogenated silicon nitride by HF using DFT [13]. We explained the continuous etching at elevated temperatures, a phenomenon that could not be explained by the simulation of crystalline Si₃N₄ [14], thus highlighting the importance of the material structure.

In the present study, we investigate the mechanism of thermal ALE of Al₂O₃ using DFT calculations, providing a comprehensive analysis covering both the fluorination by HF and the subsequent removal of the fluorinated layer by TMA. Our investigation is guided by the previous experimental results regarding the changes in surface species and the release of byproducts during thermal ALE of Al₂O₃, as schematically illustrated in Fig. 1. To simulate fluorination and removal reactions, we used amorphous Al₂O₃ (a-Al₂O₃) and amorphous AlF₃ (a-AlF₃) substrate models, respectively, due to the significant influence of crystallinity on etching reactions [13,15]. Aluminum oxide and fluoride films are amorphous at ALE process temperatures [16,17].

The amorphous models were generated by the melt-quench method using ab initio molecular dynamics (AIMD), followed by geometry optimization with DFT. For the fluorination step, we constructed the a-Al₂O₃ terminated with –OH and –CH₃ as well as fluorinated surfaces and simulated all possible pathways for successive fluorination by HF. For the removal step, we constructed an –F terminated a-AlF₃ surface model and simulated the sequential reactions involved in the removal of AlF₃ by TMA. For both fluorination and removal reactions, we evaluated and compared the reaction and activation energies at 0 K as well as the free energy changes at 250 °C for different pathways to identify the thermodynamically and kinetically favorable mechanisms. Finally, the DFT results are compared with experimental *in situ* characterization data reported in the literature [4,8,9] for validation.

2. Materials and methods

2.1. Calculation details

AIMD simulations were performed using the CP2K software package

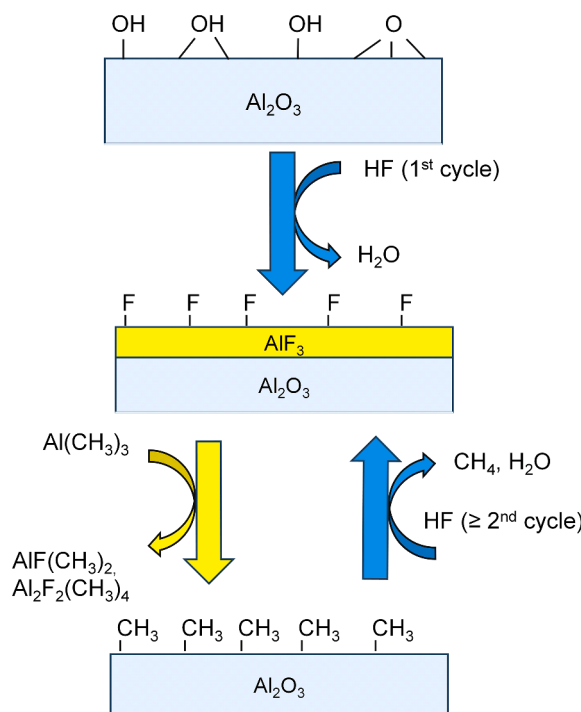


Fig. 1. Schematic of the assumed surface reactions during thermal ALE of Al₂O₃ using HF and TMA as investigated in the present study.

[18]. The generalized gradient approximation and Perdew-Burke-Ernzerhof (GGA-PBE) functional [19] and the DZVP-D3 basis set [20,21] were used to describe the exchange-correlation energy and basis functions, respectively. Simulations were performed in the NVT ensemble using the Nosé-Hoover thermostat with a time step of 1.0 fs. The density remained unchanged during the melt-quench process due to the application of the NVT ensemble.

DFT calculations were performed using the DMol³ module of the Material Studio 7.0 package (BIOVIA, USA) [22,23]. The GGA-PBE functional [19] was used together with a double numerical polarization (DNP) basis set 4.4 [22] and the DFT-D2 dispersion correction scheme [24]. Brillouin zone sampling for periodic calculations was performed using the Monkhorst-Pack method with a 2 × 2 × 1 k-point mesh, as confirmed by the convergence test shown in Fig. S1. The all-electron treatment was applied to all atoms. Other computational parameters, including smearing value, self-consistent field (SCF) convergence criteria, and geometry optimization thresholds, are identical to those used in our previous report [25] and are summarized in Table S1. Transition state geometries were located using either linear synchronous transit (LST) or quadratic synchronous transit (QST) methods [26], followed by conjugate gradient refinement as previously described [27]. The convergence threshold for the root mean square (RMS) force was set to 0.002 Ha/Å.

2.2. Surface reaction modeling

The main potential pathways for the multistep fluorination and removal reactions were modeled and simulated. Five representative states were defined for each surface reaction pathway. The unbound reactant state (UR) corresponds to a configuration in which the substrate and the incoming reactant molecule (HF or TMA) are sufficiently far apart to have negligible interaction. The reactant state (R) is a physisorbed structure in which an HF or TMA molecule is adsorbed to the surface without forming new covalent bonds. The transition state (TS) is the highest energy configuration along the reaction coordinate connecting R and P. The product state (P) represents the configuration after a surface reaction. The unbound product state (UP) represents the configuration in which the reacted surface and the byproduct molecule are sufficiently far apart to have negligible interaction. All structural data from this study are available in a public repository [28].

The physisorption energy ($E_{\text{phy},n}$), reaction energy (ΔE_n), activation energy ($E_{\text{A},n}$), and byproduct desorption energy ($E_{\text{des},n}$) for the n^{th} step of fluorination or removal reaction were calculated using the following equations.

$$E_{\text{ads},n} = E_{\text{R}n} - E_{\text{UR}n} = E_{\text{R}n} - (E_{\text{slab},n} + E_{\text{gas}}) \quad (2)$$

$$\Delta E_n = E_{\text{P}n} - E_{\text{R}n} \quad (3)$$

$$E_{\text{A},n} = E_{\text{TS}n} - E_{\text{R}n} \quad (4)$$

$$E_{\text{des},n} = E_{\text{UP}n} - E_{\text{P}n} = (E_{\text{reacted slab},n} + \sum E_{\text{byproduct}}) - E_{\text{P}n} \quad (5)$$

where $E_{\text{UR}n}$, $E_{\text{R}n}$, $E_{\text{P}n}$, $E_{\text{TS}n}$, and $E_{\text{UP}n}$ are the system energies of UR, R, P, TS, and UP of the n^{th} fluorination and removal reaction, respectively. E_{slab} and $E_{\text{reacted slab}}$ are the energies of the initial substrate and the substrate after desorption, respectively. E_{gas} and $E_{\text{byproduct}}$ are the energies of the isolated HF or TMA molecule and the resulting isolated byproduct molecules, respectively. To mimic the bulk material during the surface reaction, atoms in the bottom layer, which is approximately a quarter of the total thickness, were constrained during geometry optimization, while all other atoms were allowed to relax fully.

Thermodynamic quantities were calculated to evaluate the feasibility of the reaction at relevant temperatures. The standard enthalpy (H°) and Gibbs free energy (G°) were calculated as functions of temperature (T) based on the electronic energy (E) at 0 K by the following

equations.

$$H^\circ(T) = E + ZPE + E_v(T) + E_r(T) + E_t(T) + RT \quad (6)$$

$$G^\circ(T) = H^\circ(T) - TS^\circ(T) \quad (7)$$

Here, ZPE is the zero-point energy, and $E_v(T)$, $E_r(T)$, and $E_t(T)$ are the vibrational, rotational, and translational energy contributions, respectively, at a given T in K. R is the gas constant, and $S^\circ(T)$ is the standard entropy.

The changes in Gibbs free energy under the standard condition (ΔG°) and the representative nonstandard condition (ΔG) were calculated as a function of temperature using the following equations:

$$\Delta G^\circ(T) = G^\circ(T)_{UPn} - G^\circ(T)_{URn} \quad (8)$$

$$\Delta G(T) = \Delta G^\circ(T) + R\ln\left(\prod p_i^{c_i}\right) \quad (9)$$

where p_i is the partial pressure in atm and c_i is the reaction coefficient of the gas species i . The temperature (T) was set to 250 °C. The partial pressures of HF and TMA were assumed to be 1 Torr. In comparison, the partial pressures of any gaseous byproduct ($p_{byproduct}$) generated during fluorination or removal reactions were assumed to be 0.01 Torr because byproducts typically have significantly lower partial pressures than the precursor.

The minimum temperature for spontaneous byproduct desorption (T_s) at which $\Delta G_{des}(T)$ is zero was estimated using the following equation:

$$T_s = \frac{\Delta H_{des}(T)}{\Delta S_{des}(T) - R\ln(p_{byproduct})} = \frac{H^\circ_{UPn}(T) - H^\circ_{Pn}(T)}{S^\circ_{UPn}(T) - S^\circ_{Pn}(T) - R\ln(p_{byproduct})} \quad (10)$$

where $\Delta G_{des}(T)$ is the Gibbs free energy change for the desorption reaction, and $\Delta H^\circ_{des}(T)$ and $\Delta S^\circ_{des}(T)$ are the standard enthalpy and entropy changes.

3. Results and discussion

3.1. Construction of amorphous Al₂O₃ substrate models

To construct the amorphous Al₂O₃ models required to simulate surface reactions, a crystalline alpha-Al₂O₃ structure with a density of 3.99 g/cm³ was used as the starting structure. The lattice parameters were isotropically expanded to obtain a density of 3.00 g/cm³, corresponding to the values typically observed in amorphous alumina films deposited by ALD at 450 K [16]. An expanded 2 × 2 × 1 supercell of alpha-Al₂O₃ (Al₄₈O₇₂) was then constructed, as shown in Fig. 2(a).

The amorphization process of the expanded alpha-Al₂O₃ was performed by the melt-quench method using AIMD simulations. Starting from a crystalline configuration in Fig. 2(a), the model was heated and equilibrated at 5000 K, a temperature significantly above the experimental melting point of alpha-Al₂O₃ (2344 K). The system was held at 5000 K for 5 ps to ensure complete melting. The successful transition to a disordered liquid state was confirmed by the following indicators: an apparent loss of long-range order compared to the initial crystalline phase, quantitative agreement in short-range structural features with experimental data for molten Al₂O₃ [29] and the liquid-like behavior of the radial distribution function (RDF) spectra in Fig. 3(a), where the tail approaches unity beyond approximately 5 Å [30]. In addition, analysis of the mean squared displacement (MSD) of atoms in Fig. S3 confirms that atomic mobility becomes diffusive and unrestricted at 5000 K after approximately 1 ps, providing further evidence for liquid-like behavior [31].

Following the 5 ps melting period at 5000 K, the molten Al₂O₃ was quenched to obtain an amorphous structure. To ensure the final amorphous structure was not overly sensitive to the specific cooling procedure, the effect of different quenching protocols was evaluated by analyzing the RDFs and Al coordination number distributions of the generated models. Fig. S4(a) and Table S2 show that the choice of quenching protocol had minimal effect on the main structural features of the final amorphous Al₂O₃.

The structural variability among independently generated amorphous samples was also investigated. Ten amorphous Al₂O₃ samples were generated using slightly different quenching conditions. The molten structure was quenched to 3000 K and held for different durations ranging from 1 to 3 ps, followed by subsequent quenching to 1500 K. Despite the variations in the intermediate hold time at 3000 K, these samples exhibited highly consistent RDF peak positions and similar Al coordination number distributions, as shown in Fig. S5(a) and Table S3. These results indicate low structural variability among the independently generated samples and suggest that a single representative sample can adequately capture the structural properties of amorphous Al₂O₃. The amorphized structure obtained from such a representative quench (sample #1 in Fig. S5(a)) is shown in Fig. 2(b). Finally, the as-quenched structure was fully geometry optimized at 0 K using DFT calculations, resulting in the final a-Al₂O₃ model shown in Fig. 2(c). A root-mean-square deviation (RMSD) of 1.448 Å was calculated between the atomic positions in the structures in Fig. 2(b) and (c), indicating a structural rearrangement during the DFT geometry optimization.

Fig. 3(b) compares the RDF of the final DFT-optimized amorphous Al₄₈O₇₂ model in Fig. 2(c) with the experimental RDFs obtained from the amorphous ALD film deposited at 200 °C by total X-ray scattering [32] and the amorphous anodized alumina film by neutron scattering [33]. The average Al–O bond length, the first peak position in the RDF, is

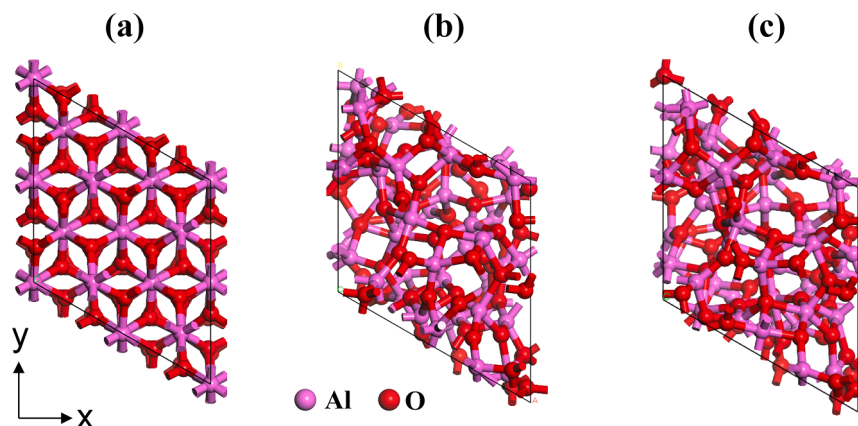


Fig. 2. Plan view atomicistic structures of the bulk phase: (a) 2 × 2 × 1 supercell of expanded alpha-Al₂O₃, Al₄₈O₇₂, (b) amorphous Al₄₈O₇₂ after melt-quenching using AIMD simulation, and (c) amorphous Al₄₈O₇₂ after geometry optimization by DFT.

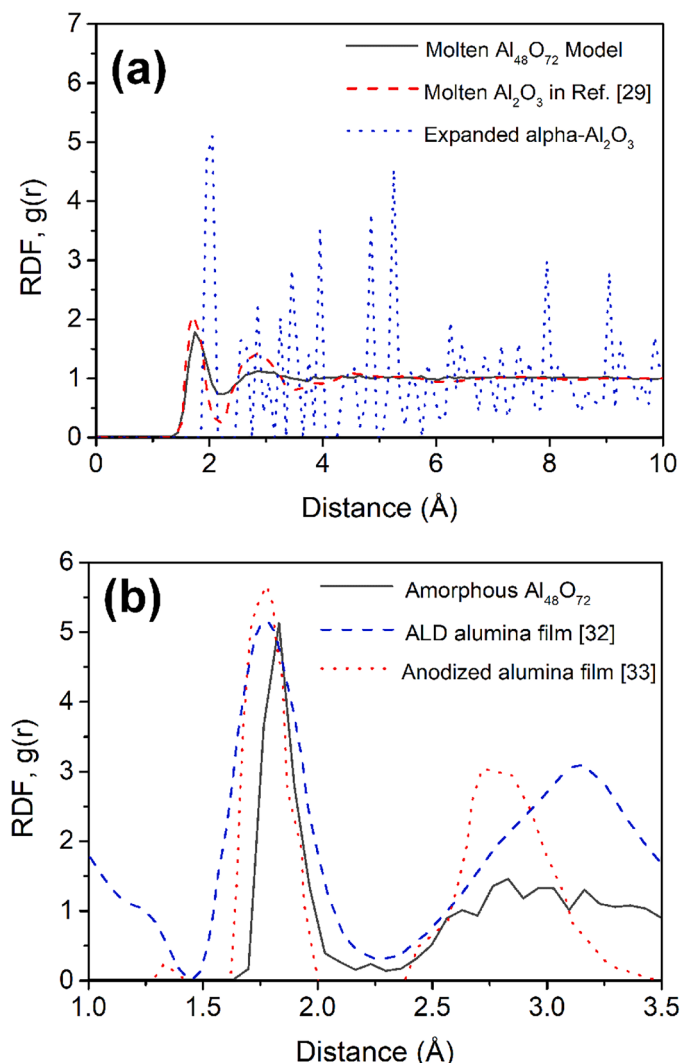


Fig. 3. RDFs calculated from AIMD simulations compared with experimental data: (a) RDF for molten $\text{Al}_{48}\text{O}_{72}$ at 5000 K (solid black lines), averaged over 40 snapshots from the last 2 ps of the AIMD simulation, compared with the RDF obtained by neutron scattering from a liquid alumina film at 2500 K (dashed red line) [29] and the calculated RDF for the initial expanded $\alpha\text{-Al}_2\text{O}_3$ (dotted blue lines). (b) RDF for the final quenched amorphous $\text{Al}_{48}\text{O}_{72}$ structure (solid black line), compared with experimental RDFs obtained from total X-ray scattering (dashed blue line) [32] or neutron scattering (dotted red line) [33] of amorphous alumina films.

$\sim 1.83 \text{ \AA}$ in our model, which is in good agreement with the experimental values of 1.75 \AA for the ALD film [32] and 1.80 \AA for the anodized film [33]. Minor discrepancies between simulated and experimental RDFs can result from differences in material properties, particularly the incorporation of impurities. For example, ALD-grown alumina films using trimethylaluminum (TMA) and H_2O at $\sim 200^\circ\text{C}$ typically contain 3–4 at% hydrogen [34], which can affect the local bonding environment and overall structure [34]. In contrast, ALD films deposited with TMA and O_3 at higher temperatures, such as 400°C , which are more representative of alumina films in semiconductor manufacturing processes, have negligible hydrogen content [34]. Recognizing that many advanced semiconductor applications require hydrogen-free alumina, our study focused on deliberately constructing a hydrogen-free amorphous alumina structure. As a result, our amorphous model shows greater structural similarity to the hydrogen-free anodized alumina reported in Ref. [33] than to the hydrogen-containing ALD film in Ref. [32].

The second broad peak in the RDF, centered at about 3.0 \AA in our model, corresponds to second-nearest-neighbor correlations, primarily Al-Al and O-O pair distances. In our model, the average Al-Al and O-O distances are 3.11 \AA and 2.74 \AA , respectively, which is in good agreement with the values from the ALD film (3.00 \AA and 2.70 \AA) [32] and the anodized film (3.20 \AA and 2.80 \AA) [33]. A notable difference, however, is the significantly larger intensity of this second peak in the experimental RDFs compared to our simulated RDF, indicating a higher degree of medium-range order (MRO) in the experimentally prepared amorphous structures [35]. This enhanced MRO is due to the much slower cooling rates typically used in the experimental fabrication of amorphous Al_2O_3 , on the order of seconds or minutes, compared to the rapid quenching rates used in AIMD simulations, which are on the order of picoseconds. Slower cooling allows for more extensive structural relaxation and promotes the development of MRO, resulting in an increased intensity of the second RDF peak [36].

Table 1 summarizes the coordination number distributions of Al atoms in our amorphous model and compares them with data from an experimental amorphous film, crystalline Al_2O_3 phases, and other reported AIMD models. Our amorphous model exhibits predominantly four- (52 %) and five-coordinated (46 %) Al atoms, with a small fraction of six-coordinated Al atoms (2 %), similar to that observed in an amorphous ALD film [37] and other AIMD models [38]. This is in sharp contrast to the crystalline forms in which $\alpha\text{-Al}_2\text{O}_3$ has exclusively six-coordinated Al atoms, while $\theta\text{-Al}_2\text{O}_3$ has equal proportions of four- and six-coordinated Al atoms.

To prepare a- Al_2O_3 slab models suitable for simulating the ALE reaction, the bulk amorphized $\text{Al}_{48}\text{O}_{72}$ structure in Fig. 2(c) was cleaved along the (0001) plane of the initial alpha-alumina structure. As a result, the amorphous $\text{Al}_{40}\text{O}_{60}$ slab model with smooth surfaces was prepared. This idealized smooth surface is considered a reasonable starting point for our simulations. For reference, atomic force microscopy (AFM) measurements on ALD alumina films have reported an RMS surface roughness of 0.148 nm before and 0.135 nm after thermal ALE using HF and TMA [15], indicating that our smooth-surfaced slab models provide a reasonable representation of the actual amorphous Al_2O_3 film.

To accurately model the surface chemistry, the surfaces of the amorphous $\text{Al}_{40}\text{O}_{60}$ slab were passivated. First, five –OH surface groups were introduced to the terminal Al atoms, and five H atoms were attached to the O atoms on both the top and bottom surfaces of the slab, resulting in the formation of five terminal OH ($\text{Al}-\text{OH}^*$) and five bridging OH ($\text{Al}-\text{O}(\text{H}^*)-\text{Al}$) groups. A vacuum region of 20 \AA was added in the z-direction (perpendicular to the slab surface) to prevent artificial interactions between the slab and its periodic images, thus ensuring realistic surface modeling under periodic boundary conditions.

The optimal –OH coverage for the top surface was then determined based on the procedure described in Ref. [39], and the structural evolution during this optimization process is shown in Fig. 4. The energetics of H_2O formation via dehydroxylation were investigated. The H_2O formation from models with ten and eight –OH surface groups was

Table 1

Coordination number distribution of Al atoms in the amorphous model generated in this work, compared with data from an experimental amorphous film, crystalline alumina phases, and previously reported AIMD models. The Al–O cutoff distance used to determine the coordination number is 2.15 \AA , which corresponds to the minimum position after the first peak in the RDF spectrum corresponding to Al–O interactions.

Structure	Coordination number of Al atom			
	4	5	6	Average
This work (a- Al_2O_3)	52 %	46 %	2 %	4.50
Amorphous ALD film [37]	55 %	42 %	3 %	4.1–4.8
Alpha- Al_2O_3	0	0	100 %	6
Theta- Al_2O_3	50 %	0	50 %	5
Other AIMD models [38]	37–48 %	42–50 %	4–5 %	4.44–4.52

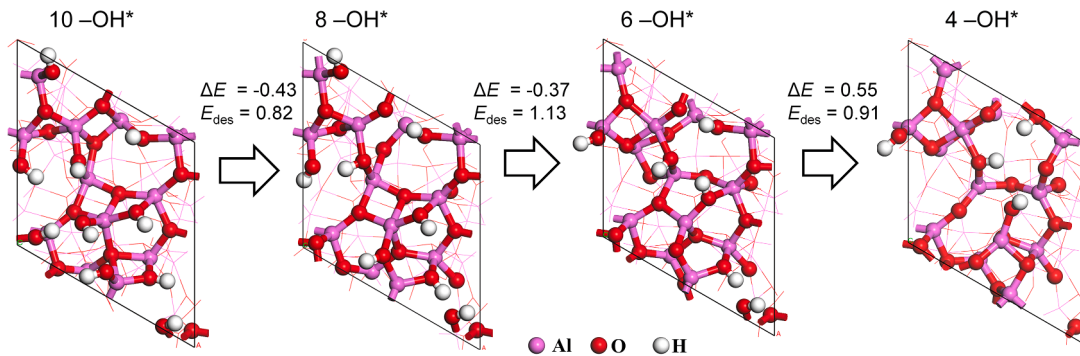


Fig. 4. Evolution of atomistic structures during optimization of surface -OH coverage on the a-Al₂O₃ slab model. The most exothermic reaction (ΔE) and desorption (E_{des}) energies are also displayed in eV.

exothermic with ΔE of -0.43 and -0.37 eV, respectively. However, further dehydroxylation was endothermic with ΔE of 0.55 eV and E_{des} of 0.91 eV, making it nonspontaneous at temperatures below 319 °C, assuming an H₂O pressure of 1 Torr. Therefore, the number of -OH groups on the top surface was set to six for simulations at the ALE process temperature of 250 °C. An equivalent coverage of six -OH groups was also formed on the bottom surface.

The final -OH terminated a-Al₂O₃ substrate model shown in Fig. 5(a) consists of 40 Al atoms, 66 O atoms, and 12 H atoms, corresponding to a surface -OH density of 6.3 OH/nm². For comparison, an amorphous film deposited by ALD at 125 °C has a surface -OH density of 8 OH/nm² [40]. It has also been reported that the surface -OH density of an amorphous film deposited by ALD at 250 °C decreased by 25% when the annealing temperature was increased from 125 °C to 250 °C [41], which is consistent with the conditions modeled in this study. In addition, to mimic surfaces exposed to TMA in the second or subsequent ALE cycles, a -CH₃ terminated surface was also constructed. Since no C-O bond peak was observed in the FTIR spectra after TMA exposure [4], only terminal -OH* groups on the model shown in Fig. 5(a) were replaced by two -CH₃ groups, while the Al-O(H*)-groups were retained. The resulting -CH₃ terminated surface is shown in Fig. 5(b).

Consistent with our previous studies on SiO₂ [42], Si [42], and SiN [13], a series of fluorinated a-Al₂O₃ slab models with increasing degrees of fluorination were also prepared to simulate the second, third, and subsurface fluorination reaction steps, as shown in Fig. 5(c), (d), and (e), respectively. The -AlF* surface groups were formed by cleavage of the Al-O bonds in the terminal -Al-OH*, bridging -Al-O(H*)-, or backbone -Al-O-linkages, and termination of the Al with F. The -AlF₂* surface groups were formed by further fluorination of partially fluorinated species such as -Al(F*)-O(H*)- or -Al(F*)-O- by cleavage of Al-O bonds. The -AlF₃* groups were also formed by further fluorination of AlF₂* in -Al(F₂*)-O(H*)- or -Al(F₂*)-O- by cleavage of Al-O bonds. However,

due to steric hindrance, only half of the -AlF₂* groups could be converted to -AlF₃*. Finally, all fluorinated substrate models were fully geometry optimized using DFT calculations to obtain energetically stable configurations.

3.2. Fluorination of amorphous aluminum oxide by HF

We simulated the sequential fluorination steps of a-Al₂O₃ with HF, forming AlF₃ and volatile byproducts. Due to the complex and disordered nature of the amorphous model, multiple potential reaction pathways were explored for each fluorination step. This approach is analogous to the methodology used in our previous publication on amorphous silicon nitride [13]. During each fluorination step, an Al-O or Al-C bond is broken upon reaction with an incoming HF molecule. Simultaneously, the F atom from HF bonds to the Al atom, forming an Al-F bond, while the H atom from HF bonds to the O or C atom on the surface, forming an O-H or C-H bond.

Table 2 summarizes the potential pathways identified for the sequential fluorination of a-Al₂O₃ with HF. The table shows the calculated physisorption energies (E_{phy}), reaction energies (ΔE), desorption energies (E_{des}), and activation energies (E_A) at 0 K, along with the Gibbs free energy changes (ΔG) at 250 °C. For each fluorination step, an incoming HF molecule first physisorbs to the surface. The calculated E_{phy} ranges from -0.25 to -0.95 eV, which can be attributed to the formation of multiple hydrogen bonds between the HF molecule and existing surface groups such as -OH_x* or -F*. As the degree of fluorination increases, physisorption becomes less favorable due to the reduction in the number of hydrogen atoms on fluorinated surfaces compared to the initial -OH terminated surfaces.

In the initial fluorination step of the -OH terminated surface of Fig. 5(a), HF was assumed to react with different surface groups of Al-OH*, AlO(H)*-Al, or AlO*-Al, resulting in the formation of AlF* together with

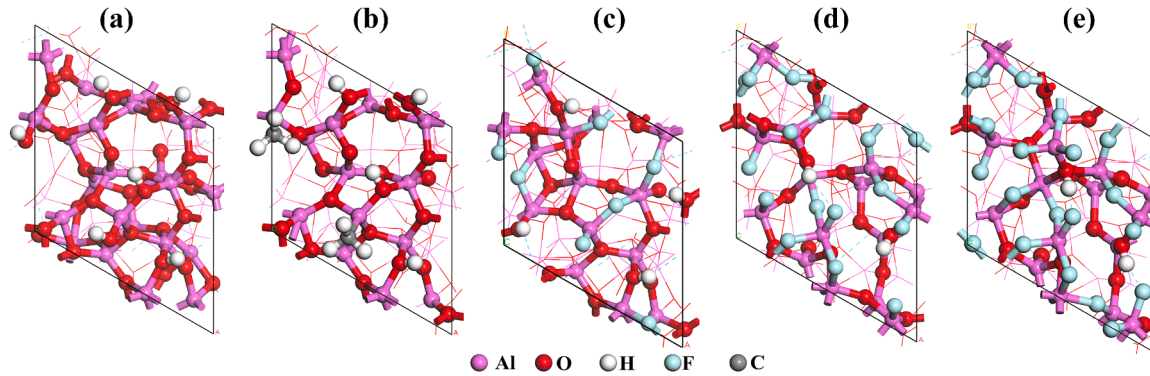


Fig. 5. Planar views of the a-Al₂O₃ substrate models used to simulate the fluorination reaction by HF, terminated with (a) -OH, (b) -CH₃, (c) -AlF, (d) -AlF₂, and (e) -AlF₃.

Table 2

Calculated energetic parameters for potential reaction pathways during sequential fluorination of a-Al₂O₃ with HF. Energies for HF physisorption (E_{phy}), reaction (ΔE), byproduct desorption (E_{des}), and activation (E_{A}) at 0 K, as well as Gibbs free energy changes (ΔG) at 250 °C, are given in eV.

Step	Path-way	Reactions	Substrate Model in Fig. 5	E_{phy}	ΔE	E_{des}	E_{A}	ΔG
1	P1a	O ₃ Al-OH* + HF → O ₃ AlF* + H ₂ O	(a)	-0.93	-0.35	0.80	0.62	-0.74
	P1b	AlO(H*)-Al + HF → AlOH ₂ * + AlF*		-0.95	-0.22	1.27	0.65	-0.25
	P1c	AlO-Al + HF → AlO(H*)-AlF*		-0.95	-0.42	-	0.18	-0.08
	P1d	O ₃ Al-CH ₃ * + HF → O ₃ Al-F* + CH ₄		-0.83	-1.33	0.17	1.14	-2.37
2	P2a	AlO(H*)-AlF* + HF → AlOH ₂ * + AlF ₂ *	(c)	-0.66	-0.58	1.10	0.58	-1.17
	P2b	Al ₂ O-AlF* + HF → Al ₂ OH* + AlF ₂ *		-0.67	-0.39	-	0.50	0.13
3	P3a	Al ₂ O-Al(F ₂ *)O(H)Al + HF → Al ₂ OH* + AlO(H)AlF ₃ *	(d)	-0.30	-0.95	-	0.83	-0.09
	P3b	Al ₂ O-Al(F ₂ *)O(H)Al + HF → Al ₂ OH* + AlOH* + AlF ₃		-0.30	1.58	0.41	2.71	0.90
4	P4	OAIO(H)-AlF ₃ * + HF → OAIOH ₂ * + FAIF ₃ *	(e)	-0.37	-0.21	0.79	0.82	-0.08

H₂O (**P1a**), AlOH₂* (**P1b**), or AlOH* (**P1c**), respectively. In addition, the reaction of HF with the Al-CH₃* of the TMA-treated surface of Fig. 5(b) was simulated, resulting in the formation of AlF* and CH₄ (**P1d**). In the second fluorination step, HF is assumed to react with AlO(H*)-AlF or Al₂O*-AlF of Fig. 5(c) to form AlF₂* and AlOH₂* (**P2a**) or Al₂OH* (**P2b**). The reactions to form **P2a** and **P2b** are mechanistically analogous to those to form **P1b** and **P1c** in the initial fluorination step, respectively. For the third fluorination step, HF was assumed to react with AlO*-AlF₂ of Fig. 5(d) to form -AlF₃* (**P3a**) or a gaseous AlF₃ molecule (**P3b**) together with AlOH*. Finally, the reaction of HF with the subsurface Al₂O₃ layer under -AlF₃* is considered, resulting in the formation of OAl-OH* and F-AlF₃* (**P4**).

Most of the pathways leading to the formation of surface-bound AlF₃* (**P1a**, **P1b**, **P1c**, **P1d**, **P2a**, **P3a**, **P4**) are calculated to be exothermic with relatively low activation energies. In addition, the calculated Gibbs free energy changes at 250 °C for these pathways are also negative, indicating that sequential surface fluorination to form AlF₃* is thermodynamically favorable at this temperature. In contrast,

the direct formation of gaseous AlF₃ in **P3b** is significantly less favorable.

Fig. 6 shows the changes in atomistic structures for four investigated pathways for the initial fluorination of a-Al₂O₃ by HF. In Fig. 6, the label “H” refers to the hydrogen atom originating from the attacking HF molecule, and the dashed lines represent the important interatomic distances in Å. The reaction involving the release of H₂O from O₃Al-OH* by HF (**P1a**) was calculated to be exothermic with a ΔE of -0.35 eV. This exothermicity is attributed to the favorable energy balance from the formation of strong Al-F (7.43 eV) and O-H (5.13 eV) bonds, which outweighs the energy required to break the H-F (6.02 eV [42]) and surface Al-O (5.94 eV) bonds. The bond dissociation energies were calculated using slab models or gas molecules. In **TS1a**, the HF molecule interacts with the O₃Al-OH* group to form a strained four-membered ring-like geometry (-Al-O-H-F-). The Al-F and O-H bonds are stretched to 2.04 Å and 1.32 Å, respectively, while the H-F and Al-O bonds are stretched by 0.10 Å and 0.13 Å, respectively, from their initial states. This configuration results in a low E_{A} of 0.62 eV. The subsequent

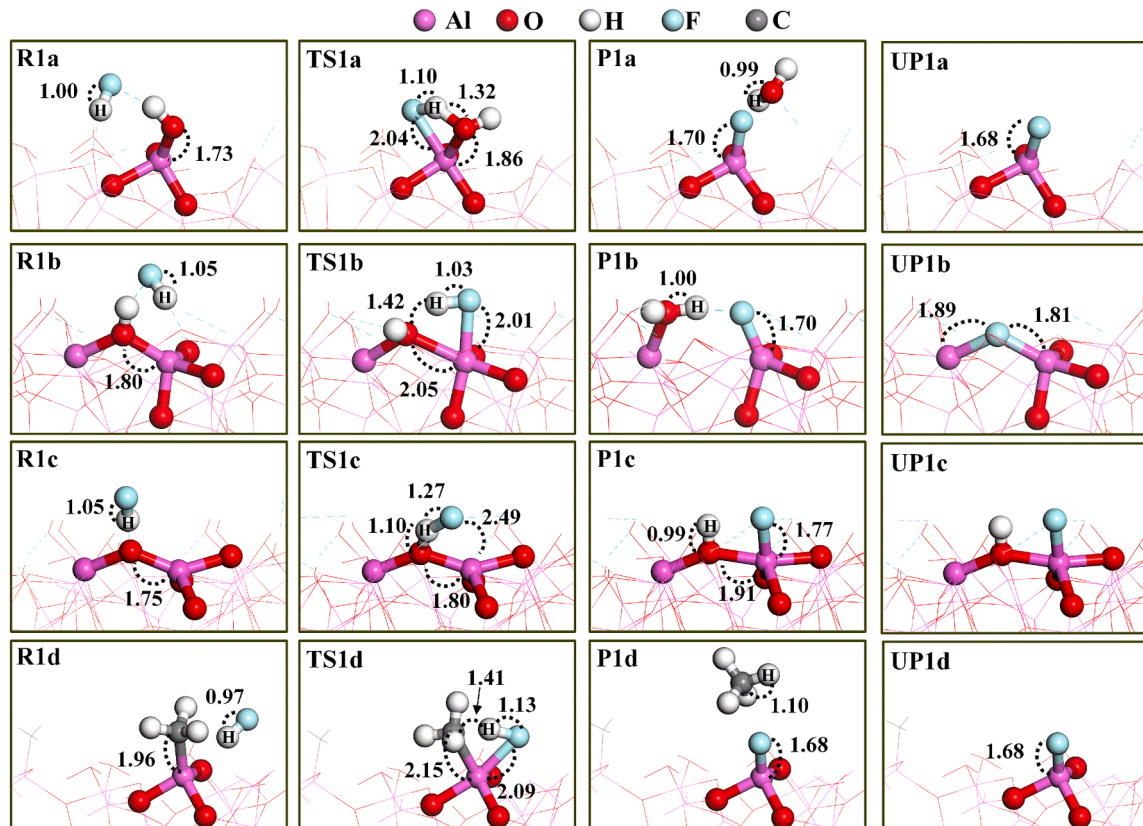


Fig. 6. Changes in atomistic structures for initial fluorination pathways of a-Al₂O₃ by HF. “H” refers to an H atom originating from the HF molecule. Dashed lines represent the important interatomic distances, with values in Å.

desorption of the byproduct H_2O is an endothermic process with an E_{des} of 0.80 eV. Based on Eq. (10), H_2O desorption is predicted to become spontaneous at temperatures above 103 °C, primarily due to the increase in entropy during gas formation.

The reaction of HF with $\text{AlO}(\text{H}^*)\text{-Al}$ (**P1b**) was also found to be exothermic with ΔE of −0.22 eV. Similar to **P1a**, this exothermicity is driven by the formation of Al–F and O–H bonds, offsetting the dissociation of H–F and Al–O bonds. In **TS1b**, an F atom of the incoming HF molecule bonds with an Al atom of $\text{AlO}(\text{H}^*)\text{-Al}$ to form an elongated Al–F bond (2.01 Å) without bond dissociation. The Al–O bond involved in the reaction was elongated by 0.25 Å compared to its initial state. The relatively low E_A of 0.65 eV was probably due to the formation of the Al–F bond despite the strain introduced by the elongation of the Al–O bond. The chemisorbed H_2O molecule in **P1b** subsequently desorbs to form Al–F–Al in **UP1b** with an E_{des} of 1.27 eV, which is predicted by Eq. (10) to occur spontaneously at temperatures higher than 142 °C.

The dissociative chemisorption of HF on the AlO–Al (**P1c**) was also calculated to be exothermic with ΔE of −0.42 eV due to the formation of Al–F and O–H bonds despite the dissociation of H–F and the generation of over-coordination of O atoms. In **TS1c**, the elongated O–H bond (1.10 Å) is formed, while the H–F and Al–O bonds are stretched by 0.22 and 0.58 Å, respectively. No dissociated bond was observed, contributing to the very low E_A of 0.18 eV.

The reaction involving the release of CH_4 from $\text{O}_3\text{Al}-\text{CH}_3^*$ by HF (**P1d**) is the most exothermic of the initial fluorination pathways, with a ΔE of −1.52 eV due to the formation of Al–F (7.43 eV) and C–H (4.59 eV) bonds overcoming the dissociation energies of H–F (6.02 eV [42]) and Al–C (4.00 eV) bonds. The higher exothermicity of this process compared to the release of H_2O (**P1a**) is mainly due to the significantly weaker Al–C bond compared to the Al–O bond. In **TS1d**, the F atom of HF begins to bond to an Al atom of $\text{O}_3\text{Al}-\text{CH}_3^*$ without cleavage of a covalent bond. An elongated Al–F bond of 2.06 Å is observed, and the Al–C bond is extended from 1.96 Å to 2.15 Å. The relatively low E_A of 1.14 eV was calculated. The desorption of the byproduct CH_4 is endothermic with an E_{des} of 0.17 eV and is predicted by Eq. (10) to be spontaneous at temperatures higher than −159 °C, suggesting easy desorption at the experimental temperature of 250 °C.

Overall, all four initial fluorination pathways (**P1a**, **P1b**, **P1c**, **P1d**) by HF involving cleavage of Al–O or Al–C were calculated to be exothermic with relatively low E_A ranging from 0.18 eV to 1.14 eV. Furthermore, the ΔG values at 250 °C were all negative, indicating that the first fluorination step is thermodynamically favorable and kinetically accessible at the experimental ALE temperature of 250 °C.

Fig. 7 illustrates the changes in atomistic structures for the two pathways investigated for the second fluorination step by HF. The cleavage of the Al–O bond of $\text{AlO}(\text{H}^*)\text{-AlF}^*$ to form AlF_2^* (**P2a**) is

exothermic with a ΔE of −0.58 eV. Pathway **P2a** involves similar bond changes as the analogous initial pathway **P1b** but is more exothermic, mainly due to the lower physisorption energy in **R2a** than in **R1b**. In **TS2a**, the F atom of HF is bonded to an Al atom of $\text{AlO}(\text{H}^*)\text{-AlF}^*$, while an Al–O bond is dissociated. An elongated Al–F bond (2.00 Å) was formed, and the H–F bond was slightly extended by 0.06 Å. The low E_A of 0.58 eV is mainly due to the energy gained from the formation of the Al–F bond, which compensates for the energy cost of dissociating the Al–O bond. A chemisorbed H_2O molecule in the **P2a** state would desorb and form an additional Al–F bond in **UP2a** with an E_{des} of 1.10 eV.

The dissociative chemisorption of HF on $\text{Al}_2\text{O}^*\text{-AlF}^*$ (**P2b**) was also calculated to be exothermic with a ΔE of −0.39 eV. Since the triple-bridged oxygen atom in **R2b** is more stable than the double-bridged oxygen in the analogous **R1c** pathway, the reaction to **P2b** is less exothermic than that of **P1c** ($\Delta E = -0.42$ eV). In **TS2b**, the HF molecule is attached to $\text{Al}_2\text{O}^*\text{-AlF}^*$, forming a four-membered ring-like geometry analogous to that observed in **TS1a**. Stretched Al–F (1.90 Å) and O–H (1.29 Å) bonds are observed, and the H–F and Al–O bonds are extended by approximately 0.18 Å. These structural changes correspond to a low E_A of 0.50 eV.

Overall, both second fluorination pathways (**P2a** and **P2b**) are exothermic, driven mainly by the formation of a strong Al–F bond, similar to the first fluorination step. The low E_A values of 0.58 and 0.50 eV suggest that the fluorinations are kinetically accessible at moderate temperatures. At 250 °C, the cleavage of $\text{AlO}(\text{H}^*)\text{-AlF}$ is predicted to be spontaneous. On the other hand, the cleavage of $\text{Al}_2\text{O}^*\text{-AlF}$ shows a slightly positive ΔG of 0.13 eV, mainly due to the decrease in entropy. Nevertheless, we considered the **P2b** pathway plausible because $-\text{AlF}_2^*$ of **P2b** is readily consumed in the subsequent third fluorination step by the reaction from **R3a** to **P3a**, as discussed in the following section.

Fig. 8 illustrates the changes in atomistic structures for two representative pathways for the third fluorination step by HF. The formation of $-\text{AlF}_3^*$ by HF (**P3a**) is more exothermic ($\Delta E = -0.95$ eV) than analogous pathways in the first (**P1b**) and second (**P2a**) steps, mainly due to the lower physisorption energy in **R3a** than in **R1b** and **R2a**. In **TS3a**, the F atom from the incoming HF molecule is bonded to the Al atom of the $\text{Al}_2\text{O}\text{-Al}(\text{F}_2^*)\text{O}(\text{H})\text{Al}$, while the Al–O bond is cleaved. The formation of an Al–F bond with a length of 1.83 Å is observed, while the H–F bond is stretched by 0.09 Å. The relatively low E_A of 0.83 eV is attributed to the energy gained from the partial formation of an Al–F bond, which partially compensates for the energy required to dissociate the Al–O bond and stretch the H–F bond.

The alternative third fluorination pathway, involving the direct release of an AlF_3 molecule from the surface (**P3b**), was calculated to be highly endothermic with ΔE of 1.58 eV due to the considerable energy cost of dissociating two Al–F and one Al–O bonds despite the energy

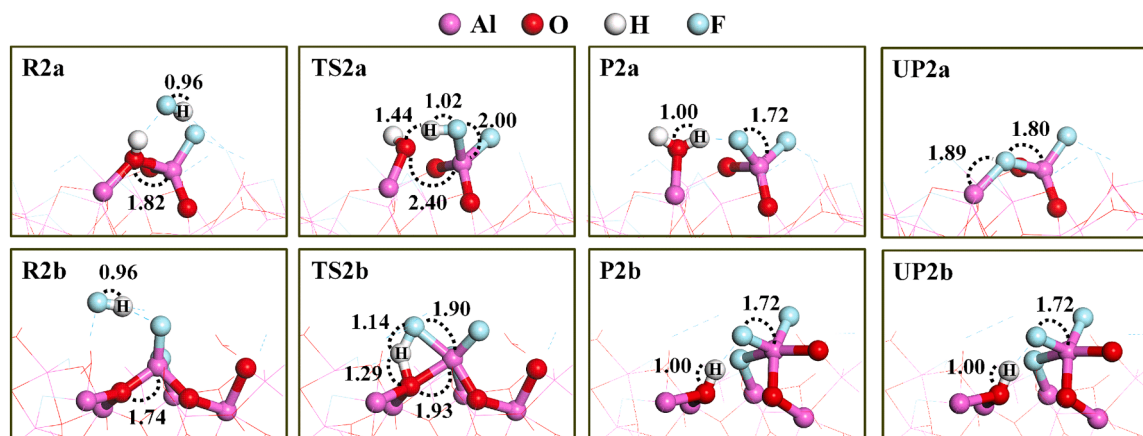


Fig. 7. Changes in the atomistic structures for the second fluorination pathways of $\alpha\text{-Al}_2\text{O}_3$ by HF. The label “H” refers to an H atom originating from the HF molecule. Dashed lines represent the important interatomic distances, with values in Å.

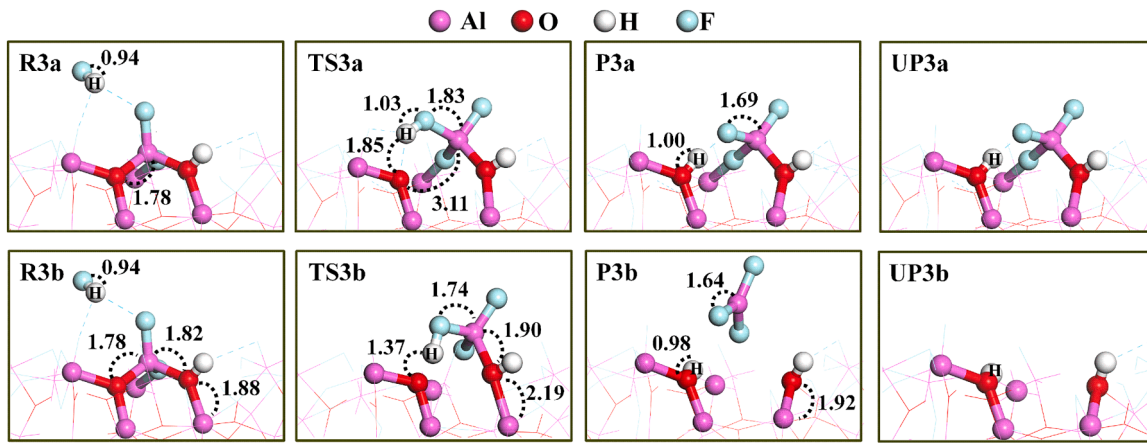


Fig. 8. Changes in atomistic structures for third fluorination pathways of a-Al₂O₃ by HF. The label “H” refers to an H atom originating from the HF molecule. Dashed lines represent the important interatomic distances, with values in Å.

gained from forming one Al–F bond and one O–H bond. In **TS3b**, one Al–F and one Al–O bond are dissociated, while an elongated Al–F bond with a length of 1.74 Å is formed, resulting in a high E_A .

Overall, the formation of surface-bound –OAlF₃* (**P3a**) is a spontaneous process with a low E_A . In contrast, the direct release of AlF₃ molecules (**P3b**) at 250 °C is predicted to be thermodynamically unfavorable, despite the increase in entropy, because it is highly endothermic.

Fig. 9 shows the changes in atomistic structure during the fluorination by HF of the subsurface region located beneath the surface –AlF₃* groups. The reaction of HF with OAl(OH)–AlF₃* in **R4** to form FAIF₃* and OAlOH* in **P4** was calculated to be exothermic with a ΔE of −0.21 eV. In **TS4**, an Al–F bond with a stretched length of 1.94 Å is formed, an Al–O bond in the subsurface dissociates, and the H–F bond is slightly stretched by 0.02 Å. These structural changes result in a low E_A of 0.82 eV. After the reaction to form **P4**, an H₂O molecule can desorb from the surface to form OAl–F–AlF₃ in **UP4** with an E_{des} of 0.79 eV. According to Eq. (10), this desorption process is spontaneous at 250 °C with ΔG of −0.08 eV, indicating the plausibility of multilayer fluorination.

Based on the results of the DFT calculations using the a-Al₂O₃ slab models, the sequential fluorination of amorphous alumina by HF is predicted to be thermodynamically favorable and kinetically accessible at 250 °C, resulting in the formation of a thin AlF₃ layer. Our computational prediction of surface Al–F bond formation is in good agreement with *in situ* FTIR and XPS observations [4,8]. In addition, the calculated release of H₂O and CH₄ molecules as byproducts is consistent with *in situ* QMS [9] and FTIR [4] observations, respectively.

Our finding that fluorination can extend into the subsurface alumina layer beneath the surface AlF₃ layer provides a theoretical explanation for the formation of multilayer aluminum fluoride observed experimentally after exposure to HF at 1 Torr or higher pressure [43].

In the following subsections, we present the modeling and simulation results for the removal reaction of the formed AlF₃ layer by TMA.

3.3. Construction of amorphous AlF₃ substrate models

Amorphous AlF₃ substrate models were constructed using a method similar to that described for the amorphous Al₂O₃ models. The starting structure was alpha-AlF₃, with an experimental bulk density of 3.26 g/cm³. Before melting, the lattice dimensions were isotropically increased to adjust the model density to 2.90 g/cm³, which was chosen to match the reported density of amorphous AlF₃ films deposited by ALD at 423 K [17]. A 2 × 2 × 1 expanded alpha-AlF₃ supercell (Al₂₄F₇₂) was then constructed, as shown in **Fig. 10(a)**.

The amorphous structure was generated by the melt-quench method via AIMD simulation. The heating and initial cooling steps were identical to the a-Al₂O₃ case, but an additional 1 ps duration at 750 K was added at the end of the cooling protocol due to the lower melting point of AlF₃ compared to Al₂O₃. The successful transition to the liquid state during the melting phase was confirmed by criteria analogous to those used for a-Al₂O₃, that is, comparison of the RDF of molten AlF₃ with that of alpha AlF₃ (**Fig. S2**) and analysis of the atomic displacement evolution during the simulation (**Fig. S3**). The influence of different quenching protocols on the final amorphous AlF₃ structure was found to be minimal, as evidenced by the consistent RDFs shown in **Fig. S4(b)**. Furthermore, ten independent amorphous AlF₃ samples generated by quenching a molten structure at 3000 K for different durations ranging from 1 to 3 ps, followed by quenching to 1500 K and then to 750 K, exhibited consistent RDF peak positions as shown in **Fig. S5(b)**, indicating low structural variability among independently generated samples. This suggests that a single representative sample may be sufficient to represent the structural properties of amorphous AlF₃. The amorphized structure of such a representative sample (#1 from **Fig. S5(b)**) is shown in **Fig. 10(b)**. Finally, this as-quenched structure was fully geometry optimized at 0 K using DFT calculations, resulting in the final structure of a-AlF₃ shown in **Fig. 10(c)**.

To simulate the ALE reaction on a-AlF₃ substrates, the amorphized bulk structure in **Fig. 10(c)** was cleaved along the (0001) plane of the

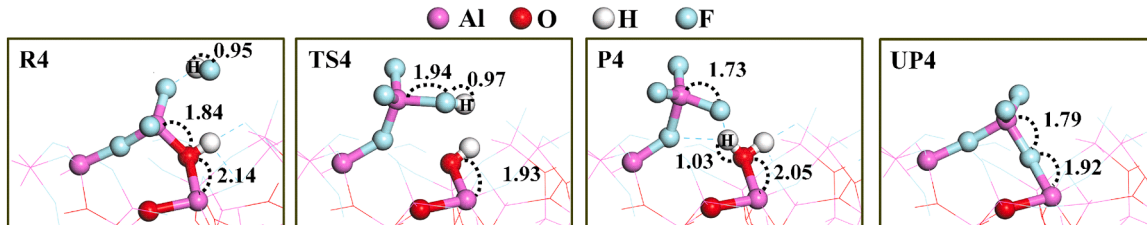


Fig. 9. Changes in atomistic structures for the subsurface fluorination of a-Al₂O₃ by HF. “H” refers to an H atom originating from the HF molecule. Dashed lines represent the important interatomic distances, with values in Å.

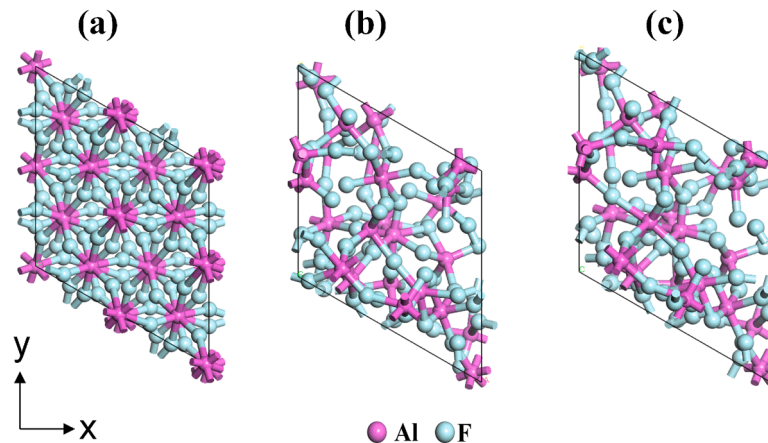


Fig. 10. Plan view atomistic structures of the bulk phase: (a) the initial $2 \times 2 \times 1$ supercell of expanded alpha- AlF_3 , $\text{Al}_{24}\text{F}_{72}$, (b) the amorphous $\text{Al}_{24}\text{F}_{72}$ structure after melt-quenching using AIMD simulation, and (c) the final amorphous $\text{Al}_{24}\text{F}_{72}$ after geometry optimization by DFT.

initial alpha AlF_3 structure, resulting in the $\text{Al}_{24}\text{F}_{72}$ slab model with relatively smooth surfaces. To mimic the AlF_3 surface after HF exposure, three F atoms were attached to the surface-exposed Al atoms, forming $\text{Al}-\text{F}^*$ groups, while three H atoms were attached to the F atoms on the top and bottom surfaces of the slab model, forming $\text{Al}-\text{FH}^*$ groups. A vacuum region of 20 Å was inserted between the periodic slabs.

The optimal surface coverage of $-\text{FH}^*$ groups on the top surface was determined by simulating the spontaneous release of HF molecules, analogous to the $-\text{OH}^*$ optimization performed for the a- Al_2O_3 model. The changes in the atomistic structures are shown in Fig. 11. The release of the first HF molecule from the model, initially containing three $-\text{FH}^*$ groups, was calculated to be exothermic with ΔE of -0.11 eV. In contrast, the subsequent releases of the additional HF molecules were found to be endothermic, with ΔE of 0.49 and 0.71 eV, respectively. Despite their endothermic nature, these HF desorption events are predicted to occur spontaneously at temperatures above -30 and 129 °C, respectively. Therefore, we expected no residual $-\text{FH}^*$ groups on the a- AlF_3 surface at the ALE processing temperature of 250 °C. The presence of minimal HF molecules on the fluorinated Al_2O_3 surface has been observed after exposure to HF at 200 °C or higher [44], which supports our prediction. The final a- AlF_3 substrate model, representing the surface after complete fluorination by HF, consists of 24 Al and 72 F atoms, as shown in Fig. 12(a).

Considering that the removal reaction by TMA is also a multistep process, a $-\text{CH}_3^*$ terminated AlF_3 substrate model was also prepared by replacing the surface F atoms with CH_3 groups to simulate the second step of the removal reaction, as shown in Fig. 12(b). After this modification, the $-\text{CH}_3^*$ terminated a- AlF_3 substrate model was subjected to

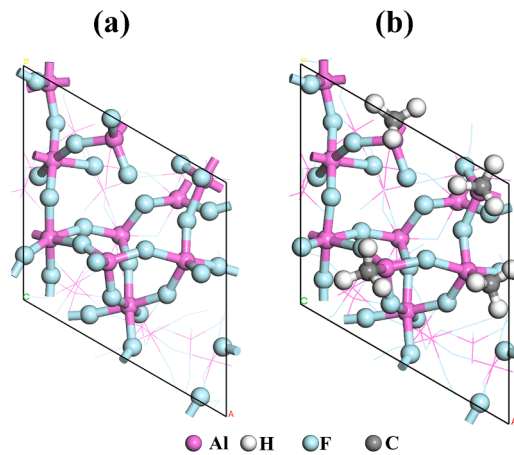


Fig. 12. Planar views of the a- AlF_3 substrate models used to simulate the TMA removal reactions: (a) -F terminated and (b) $-\text{CH}_3$ terminated models.

geometry optimization by DFT calculations.

3.4. Removal reactions of amorphous AlF_3 by TMA

For the removal reactions of a- AlF_3 by TMA, we assumed that dimethylaluminum fluoride ($\text{Al}(\text{CH}_3)_2\text{F}$, DMAF) would be the primary aluminum-containing volatile byproduct molecules. Both TMA and

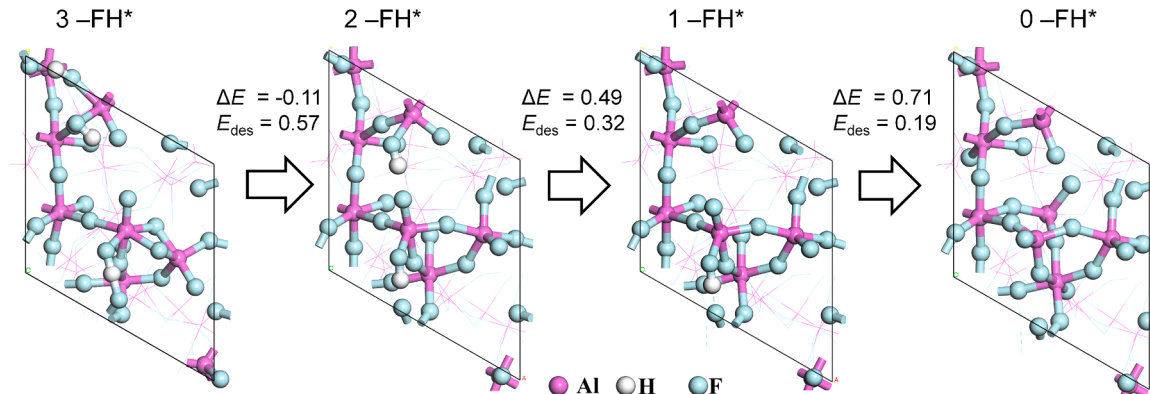


Fig. 11. Evolution of atomistic structures during the optimization of surface $-\text{FH}$ coverage on the a- AlF_3 slab model. The most exothermic reaction (ΔE) and desorption (E_{des}) energies are also displayed in eV.

DMAF are known to exist as either monomers or dimers, depending on the temperature [9,45]. To determine the likely state of these species under typical ALE conditions, we predicted the degree of dimer dissociation for TMA and DMAF in the gas phase as a function of temperature using DFT, as shown in Fig. 13. The total pressures of TMA and DMAF were assumed to be 1 and 0.01 Torr, respectively, representing typical precursor and by-product partial pressures. At 250 °C, the TMA dimer was predicted to dissociate almost completely into monomers, so TMA was treated as a monomer in subsequent calculations. On the other hand, the dissociation behavior of DMAF dimers depends on their bridging structure. Three dimer structures of DMAF were considered, each with two F-bridges, one F-bridge and one CH₃-bridge, and two CH₃-bridges. DFT calculations indicated that at 250 °C, less than 5 % of DMAF molecules with two F-bridges are predicted to dissociate, while those with other structures would dissociate completely. Therefore, when two DMAF monomers meet at 250 °C, they are likely to form a DMAF dimer with two F-bridges.

We then simulated the two-step removal reaction of a-AlF₃ by two successive TMA molecules, forming a monomer or dimer of DMAF, as shown in Table 3. Fig. 14 shows the corresponding changes in the atomistic structure. In the first removal step (P5), an incoming TMA monomer reacts with -AlF* to form -Al(CH₃)^{*} and release a DMAF monomer. This reaction was calculated to be exothermic with a ΔE of -0.51 eV, primarily because the newly formed Al-F bond in DMAF (7.19 eV) is stronger than the original Al-F bond in a-AlF₃ (7.03 eV), despite no change in the net number of bond types. In TS5, the Al atom of TMA bonds to the F atom of -AlF* to form an elongated Al-F bond of 2.07 Å, while an original subsurface Al-F bond is dissociated. As a result, a low E_A of 0.23 eV was obtained because there was no net change in bond types.

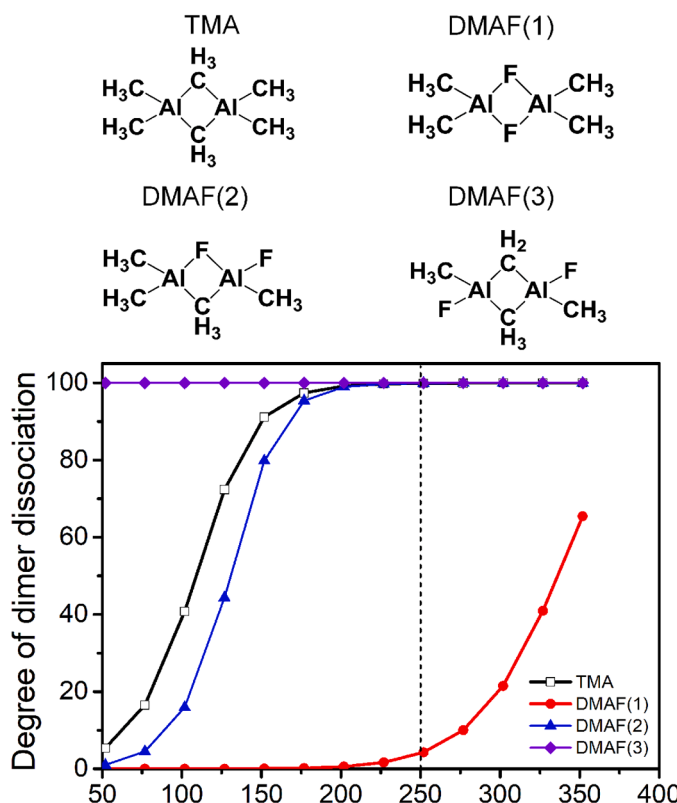


Fig. 13. Calculated degree of dimer dissociation for TMA and DMAF as a function of temperature. For DMAF, three dimer structures were considered, each with two F-bridges, one F-bridge and one CH₃-bridge, and two CH₃-bridges. The total pressures of TMA and DMAF were assumed to be 1 and 0.01 Torr, respectively.

In the second removal step (R6), a second TMA molecule reacts with (Al-F)₃-AlCH₃^{*}, a surface site created in R5, releasing a DMAF dimer as a volatile byproduct. Similar to the first step (P5), this reaction was calculated to be exothermic with ΔE of -0.24 eV. The exothermicity is primarily attributed to the formation of a stable dimer despite no net bond change. In TS6, the incoming TMA molecule interacts with the surface, dissociating three Al-F bonds from a-AlF₃ and nearly forming two new Al-F bonds that will become part of the desorbing DMAF dimer. The calculated E_A for this step was 1.08 eV.

We also modeled several potential reactions between a DMAF monomer and another DMAF monomer, TMA, or DMAF dimer on the surface to form a DMAF dimer (Al₂F₂(CH₃)₄), DMAF-TMA complex (Al₂F(CH₃)₅), or DMAF trimer (Al₃F₃(CH₃)₆), respectively, as shown in Table S4. The changes in atomistic structure are shown in Fig. S6. Both reactions between a DMAF monomer with another DMAF monomer and a DMAF dimer are exothermic and spontaneous at 250 °C with ΔG of -0.23 and -0.08 eV, respectively, indicating that the dimerization and trimerization of DMAF on the surface are favorable. The reaction between DMAF and TMA monomers is also exothermic. However, its ΔG value at 250 °C is slightly positive, suggesting that a higher TMA precursor pressure than our assumption is required to form Al₂F(CH₃)₅. These results explain the detection of Al₂F₂(CH₃)₄, Al₂F(CH₃)₅, and Al₃F₃(CH₃)₆ and the absence of the DMAF monomer in the QMS spectra [9].

The removal of an AlF₃ layer during ALE eventually exposes the underlying oxyfluoride interface region between AlF₃ and bulk Al₂O₃. Therefore, we also simulated the removal reactions of the oxyfluoride by TMA, as summarized in Table 4. Two types of surface groups of -OAlF₃^{*} and -O₂AlF₂^{*} represent the oxyfluorides on a-Al₂O₃ with high and low fluorine densities, respectively. The changes in atomistic structure are shown in Figs. S7 and S8. For the high fluorine density site of -OAlF₃^{*}, the two-step removal reaction was exothermic and spontaneous at 250 °C. The first step (P7) has a very low E_A of 0.03 eV, while the second step (P8) has a higher E_A of 1.15 eV. This indicates that TMA can remove AlF₃ from -OAlF₃^{*}, although the overall reaction would be slower than that with a-AlF₃ due to the higher barrier for P8 (1.15 eV) compared to that for P6 on pure a-AlF₃ (1.08 eV).

In contrast, the removal reaction from the lower fluorine density oxyfluoride site of -O₂AlF₂^{*} proceeds differently. Although the first TMA reaction step (P9) is exothermic, spontaneous at 250 °C, and has a low E_A of 0.29 eV, the second step (P10) was calculated to be endothermic and nonspontaneous at 250 °C. Furthermore, P10 has a relatively high E_A of 1.69 eV. These results suggest that the reaction of TMA with -O₂AlF₂^{*} would only replace fluorine with a -CH₃ group without removing Al atoms from the substrate.

The results of our DFT calculations indicate that the removal of the a-AlF₃ layer and highly fluorinated oxyfluoride sites by TMA is thermodynamically favorable and kinetically accessible at 250 °C, resulting in the release of both the monomer and dimer of DMAF. Conversely, the removal of Al from less fluorinated oxyfluoride sites is thermodynamically unfavorable and kinetically hindered at 250 °C, resulting in the formation of -CH₃^{*} termination on the surface instead of etching. Therefore, the overall removal reaction is predicted to be self-limiting, as TMA effectively removes AlF₃ and highly fluorinated oxyfluoride layers, but the etching reaction stops upon encountering the less fluorinated oxide interface. In addition, this result explains the increase in the CH₃ peak observed in the FTIR spectra [4] and the detection of carbon in the film by XPS spectra [8] after TMA exposure during Al₂O₃ ALE.

In summary, our DFT calculation provides comprehensive mechanistic insights that successfully explain the thermal ALE of alumina films by HF and TMA. This study highlights the importance of using amorphous slab models with optimized surface group densities to simulate the etching process accurately. Key mechanistic findings include the plausibility of multilayer AlF₃ formation extending beyond the immediate surface during the HF fluorination step, as well as the energetic

Table 3

Calculated energetic parameters for the two-step removal reaction of a-AlF₃ by TMA. Energies for TMA physisorption (E_{phy}), reaction (ΔE), byproduct desorption (E_{des}), and activation (E_{A}) at 0 K, as well as Gibbs free energy changes at 250 °C (ΔG), are given in eV.

Step	Path-way	Reactions	Substrate Model (Fig. 12)	E_{phy}	ΔE	E_{des}	E_{A}	ΔG
1	P5	(AlF) ₃ Al-F* + Al(CH ₃) ₃ → (AlF) ₃ AlCH ₃ * + AlF(CH ₃) ₂	(a)	-0.28	-0.51	0.22	0.23	-0.87
2	P6	(Al-F) ₃ -AlCH ₃ * + Al(CH ₃) ₃ → -Al + -Al ₂ F* + Al ₂ F ₂ (CH ₃) ₄	(b)	-0.38	-0.24	0.40	1.08	-0.85

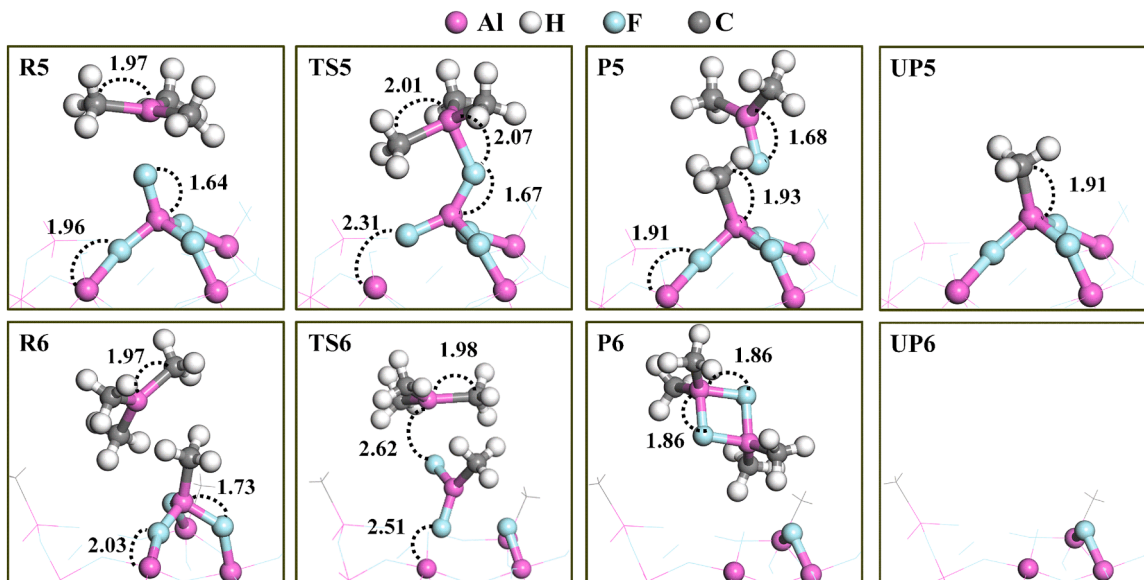


Fig. 14. Changes in atomistic structures during the two-step removal reaction of a-AlF₃ by TMA. Dashed lines represent the main interatomic distances in Å.

Table 4

Calculated energetic parameters for the two-step removal reaction of aluminum oxyfluoride by TMA. Energies for TMA physisorption (E_{phy}), reaction (ΔE), byproduct desorption (E_{des}), and activation (E_{A}) at 0 K, as well as Gibbs free energy changes at 250 °C (ΔG), are given in eV.

Step	Path-way	Reactions	Substrate Model	E_{phy}	ΔE	E_{des}	E_{A}	ΔG
1	P7	-OAlF ₃ *						
2	P8	AIO(H)(AlF)AlF ₂ * + Al(CH ₃) ₃ → AIO(H)(AlF)AlFCH ₃ * + AlF(CH ₃) ₂ AIO(H)(Al-F)-AlFCH ₃ * + Al(CH ₃) ₃ → AIOH* + Al* + Al ₂ F ₂ (CH ₃) ₄ -O ₂ AlF ₂ *	Fig. 5(e) UP7 in Fig. S2	-0.55 -0.29	-0.15 -0.05	0.26 0.71	0.03 1.15	-0.63 -0.31
1	P9	AIO(H)(AlF)AlF* + Al(CH ₃) ₃ → AIO(H)(AlF)AlCH ₃ * + AlF(CH ₃) ₂	Fig. 5(d)	-0.71	-0.99	0.68	0.29	-0.83
2	P10	Al-F* + AIO(H)(Al-F)-AlCH ₃ * + Al(CH ₃) ₃ → 2Al* + AIOH* + Al ₂ F ₂ (CH ₃) ₄	UP9 in Fig. S3	-0.11	1.59	0.65	1.69	1.72

significance of the formation of aluminum-containing dimer byproducts during the TMA removal step, which is consistent with experimental observations. The detailed modeling approach presented in this study provides a foundation that can be extended to study the thermal ALE processes of other metal oxide films.

However, this study was primarily based on time-independent DFT calculations at 0 K, and the free energy at elevated temperatures was estimated using vibrational properties. As a result, the dynamic process, such as the diffusion of HF or complex surface reconstructions occurring on longer time scales, could not be elucidated. The study of such phenomena would require large-scale calculations using methods such as MD simulations. However, the development and validation of reliable interatomic potentials for these fluorine-containing material systems remain important challenges.

4. Conclusions

The mechanism of thermal ALE of aluminum oxide by HF and TMA was investigated using DFT calculations. Amorphous Al₂O₃ and AlF₃ slab models were constructed through AIMD melt-quench simulations,

optimized by DFT calculations, and used to simulate successive fluorination by HF and subsequent removal reactions by TMA. The slab models were passivated by surface groups with optimized surface coverage. The main fluorination pathways leading to the formation of multilayer AlF₃ were calculated to be spontaneous at 250 °C, with low activation energies ranging from 0.18 to 1.14 eV, releasing H₂O and CH₄ gases as volatile byproducts. Similarly, the removal reactions on a-AlF₃ by TMA, releasing the dimer of the DMAF molecule, were also found to be spontaneous at 250 °C with low activation energies up to 1.08 eV. The results indicate that the thermal ALE of Al₂O₃ is thermodynamically favorable and kinetically feasible at 250 °C. In addition, the removal of Al from less fluorinated oxyfluoride sites by TMA was nonspontaneous, with a high activation energy of 1.69 eV, indicating that the removal step is a self-limiting process. These results align well with experimental observations from *in situ* QMS, FTIR, and XPS in the literature. Our DFT calculations using realistic amorphous slab models successfully explain the fundamental surface chemistry governing the thermal ALE of aluminum oxide films.

CRediT authorship contribution statement

Khabib Khumaini: Writing – original draft, Visualization, Validation, Methodology, Investigation, Formal analysis, Data curation, Conceptualization. **Gyejun Cho:** Writing – review & editing, Visualization, Validation. **Hyun-Sub Kim:** Writing – review & editing, Visualization, Validation, Conceptualization. **Won-Jun Lee:** Writing – review & editing, Validation, Supervision, Resources, Project administration, Methodology, Funding acquisition, Conceptualization.

Declaration of competing interest

The authors declare that they have no known competing financial interests or personal relationships that could have appeared to influence the work reported in this paper.

Acknowledgment

This work was supported by the Technology Innovation Program (Public-private joint investment semiconductor R&D program(K-CHIPS) to foster high-quality human resources) (RS-2023-00232258) funded by the Ministry of Trade, Industry & Energy (MOTIE, Korea) (1415187368). This research was also partly supported by the Korea Basic Science Institute (National Research Facilities and Equipment Center) grant funded by the Ministry of Education (2022R1A6C101A774).

Supplementary materials

Supplementary material associated with this article can be found, in the online version, at [doi:10.1016/j.surfin.2025.107114](https://doi.org/10.1016/j.surfin.2025.107114).

Data availability

The raw data required to reproduce the above findings are available to download from 10.5281/zenodo.15323240.

References

- [1] S.M. George, Atomic layer deposition: an overview, Chem. Rev. 110 (2010) 111–131, <https://doi.org/10.1021/cr900056b>.
- [2] S.M. George, Mechanisms of thermal atomic layer etching, Acc. Chem. Res. 53 (2020) 1151–1160, <https://doi.org/10.1021/acs.accounts.0c00084>.
- [3] Y. Lee, S.M. George, Atomic layer etching of Al₂O₃ using sequential, self-limiting thermal reactions with Sn(acac)₂ and hydrogen fluoride, ACS Nano 9 (2015) 2061–2070, <https://doi.org/10.1021/nn507277f>.
- [4] Y. Lee, J.W. DuMont, S.M. George, Trimethylaluminum as the metal precursor for the atomic layer etching of Al₂O₃ using sequential, self-limiting thermal reactions, Chem. Mater. 28 (2016) 2994–3003, <https://doi.org/10.1021/acs.chemmater.6b00111>.
- [5] Y. Lee, S.M. George, Thermal atomic layer etching of Al₂O₃, HfO₂, and ZrO₂ using sequential hydrogen fluoride and dimethylaluminum chloride exposures, J. Phys. Chem. C 123 (2019) 18455–18466, <https://doi.org/10.1021/acs.jpcc.9b04767>.
- [6] A.M. Cano, J.L. Partridge, S.M. George, Thermal atomic layer etching of Al₂O₃ using sequential HF and BC₃ exposures: evidence for combined ligand-exchange and conversion mechanisms, Chem. Mater. 34 (2022) 6440–6449, <https://doi.org/10.1021/acs.chemmater.2c01120>.
- [7] V. Sharma, S.D. Elliott, T. Blomberg, S. Haukka, M.E. Givens, M. Tuominen, M. Ritala, Thermal atomic layer etching of aluminum oxide (Al₂O₃) using sequential exposures of niobium pentafluoride (NbF₅) and carbon tetrachloride (CCl₄): a combined experimental and density functional theory study of the etch mechanism, Chem. Mater. 33 (2021) 2883–2893, <https://doi.org/10.1021/acs.chemmater.1c00142>.
- [8] J. Reif, M. Knaut, S. Killge, M. Albert, T. Mikolajick, J.W. Bartha, *In situ* studies on atomic layer etching of aluminum oxide using sequential reactions with trimethylaluminum and hydrogen fluoride, J. Vac. Sci. Technol. A 40 (2022) 032602, <https://doi.org/10.1116/6.0001630>.
- [9] J.W. Clancey, A.S. Cavanagh, J.E.T. Smith, S. Sharma, S.M. George, Volatile etch species produced during thermal Al₂O₃ atomic layer etching, J. Phys. Chem. C 124 (2020) 287–299, <https://doi.org/10.1021/acs.jpcc.9b06104>.
- [10] S. Kondati Natarajan, S.D. Elliott, Modeling the chemical mechanism of the thermal atomic layer etch of aluminum oxide: a density functional theory study of reactions during HF exposure, Chem. Mater. 30 (2018) 5912–5922, <https://doi.org/10.1021/acs.chemmater.8b01930>.
- [11] X. Hu, J. Schuster, Chemical mechanism of AlF₃ etching during AlMe₃ exposure: a thermodynamic and DFT study, J. Phys. Chem. C 126 (2022) 7410–7420, <https://doi.org/10.1021/acs.jpcc.2c00158>.
- [12] Y. Lee, C. Huffman, S.M. George, Selectivity in thermal atomic layer etching using sequential, self-limiting fluorination and ligand-exchange reactions, Chem. Mater. 28 (2016) 7657–7665, <https://doi.org/10.1021/acs.chemmater.6b02543>.
- [13] K. Khumaini, Y. Kim, R. Hidayat, T. Chowdhury, H.-L. Kim, B. Cho, S. Park, W.-J. Lee, Etching mechanism of amorphous hydrogenated silicon nitride by hydrogen fluoride, Appl. Surf. Sci. 654 (2024) 159414, <https://doi.org/10.1016/j.apsusc.2024.159414>.
- [14] T. Chowdhury, R. Hidayat, H.-L. Kim, T.R. Mayangsari, S. Cho, S. Park, J. Jung, W.-J. Lee, Density functional theory study on the modification of silicon nitride surface by fluorine-containing molecules, Appl. Surf. Sci. 554 (2021) 149481, <https://doi.org/10.1016/j.apsusc.2021.149481>.
- [15] J.A. Murdzek, A. Rajashekhar, R.S. Makala, S.M. George, Thermal atomic layer etching of amorphous and crystalline Al₂O₃ films, J. Vac. Sci. Technol. A 39 (2021) 042602, <https://doi.org/10.1116/6.0000995>.
- [16] M.D. Groner, F.H. Fabreguette, J.W. Elam, S.M. George, Low-temperature Al₂O₃ atomic layer deposition, Chem. Mater. 16 (2004) 639–645, <https://doi.org/10.1021/cm0304546>.
- [17] Y. Lee, J.W. DuMont, A.S. Cavanagh, S.M. George, Atomic layer deposition of AlF₃ using trimethylaluminum and hydrogen fluoride, J. Phys. Chem. C 119 (2015) 14185–14194, <https://doi.org/10.1021/acs.jpcc.5b02625>.
- [18] T.D. Kühne, M. Iannuzzi, M. Del Ben, V.V. Rybkin, P. Seewald, F. Stein, T. Laino, R. Z. Khalilli, O. Schütt, F. Schiffmann, D. Golze, J. Wilhelm, S. Chulkov, M. H. Bani-Hashemian, V. Weber, U. Borstnik, M. Taillefumier, A.S. Jakobovits, A. Lazzaro, H. Pabst, T. Müller, R. Schade, M. Guidon, S. Andermatt, N. Holmberg, G.K. Schenter, A. Hehn, A. Bussy, F. Belleflamme, G. Tabacchi, A. Glöb, M. Lass, I. Bethune, C.J. Mundy, C. Plessl, M. Watkins, J. VandeVondele, M. Krack, J. Hutter, CP2K: an electronic structure and molecular dynamics software package - Quickstep: efficient and accurate electronic structure calculations, J. Chem. Phys. 152 (2020) 194103, <https://doi.org/10.1063/5.0007045>.
- [19] J.P. Perdew, K. Burke, M. Ernzerhof, Generalized gradient approximation made simple, Phys. Rev. Lett. 77 (1996) 3865–3868, <https://doi.org/10.1103/PhysRevLett.77.3865>.
- [20] J. VandeVondele, J. Hutter, Gaussian basis sets for accurate calculations on molecular systems in gas and condensed phases, J. Chem. Phys. 127 (2007) 114105, <https://doi.org/10.1063/1.2770708>.
- [21] S. Grimme, J. Antony, S. Ehrlich, H. Krieg, A consistent and accurate *ab initio* parametrization of density functional dispersion correction (DFT-D) for the 94 elements H–Pu, J. Chem. Phys. 132 (2010) 154104, <https://doi.org/10.1063/1.3382344>.
- [22] B. Delley, An all-electron numerical method for solving the local density functional for polyatomic molecules, J. Chem. Phys. 92 (1990) 508–517, <https://doi.org/10.1063/1.458452>.
- [23] B. Delley, From molecules to solids with the DMol3 approach, J. Chem. Phys. 113 (2000) 7756–7764, <https://doi.org/10.1063/1.1316015>.
- [24] S. Grimme, Semiempirical GGA-type density functional constructed with a long-range dispersion correction, J. Comput. Chem. 27 (2006) 1787–1799, <https://doi.org/10.1002/jcc.20495>.
- [25] K. Khumaini, H. Roh, H. Han, H.-L. Kim, H.-S. Kim, J.-H. Seok, J.W. Park, W.-J. Lee, Surface reaction mechanism of atomic layer deposition of niobium oxide: *in situ* characterization and first-principle study, Appl. Surf. Sci. 615 (2023) 156340, <https://doi.org/10.1016/j.apsusc.2023.156340>.
- [26] N. Govind, M. Petersen, G. Fitzgerald, D. King-Smith, J. Andzelm, A generalized synchronous transit method for transition state location, Comput. Mater. Sci. 28 (2003) 250–258, [https://doi.org/10.1016/S0927-0256\(03\)00111-3](https://doi.org/10.1016/S0927-0256(03)00111-3).
- [27] K. Khumaini, R. Hidayat, T.R. Mayangsari, T. Chowdhury, H.-L. Kim, S.-I. Lee, W.-J. Lee, Density functional theory study on the selective capping of cobalt on copper interconnect, Appl. Surf. Sci. 585 (2022) 152750, <https://doi.org/10.1016/j.apsusc.2022.152750>.
- [28] K. Khumaini, G. Cho, H.-L. Kim, W.-J. Lee, Thermal atomic layer etching of aluminum oxide by hydrogen fluoride and trimethylaluminum: first-principles study [Data set], Zenodo (2025), <https://doi.org/10.5281/zenodo.15323240>.
- [29] C. Landron, A.K. Soper, T.E. Jenkins, G.N. Greaves, L. Hennet, J.P. Coutures, Measuring neutron scattering structure factor for liquid alumina and analysing the radial distribution function by empirical potential structural refinement, J. Non-Cryst. Solids 293–295 (2001) 453–457, [https://doi.org/10.1016/S0022-3093\(01\)00839-0](https://doi.org/10.1016/S0022-3093(01)00839-0).
- [30] M.P. Allen, D.J. Tildesley, Computer Simulation of Liquids, 2nd Edition, Oxford University Press, Oxford, 2017, <https://doi.org/10.1093/oso/9780198803195.001.0001>.
- [31] Y. Wang, G. Zhao, C. Liu, Z. Zhu, Ab initio molecular dynamics simulations on structural change of supercooled liquid Si at different temperatures from 1700 to 1100K, Physica B 406 (2011) 3991–3996, <https://doi.org/10.1016/j.physb.2011.07.062>.
- [32] A. Pugliese, B. Shyam, G.M. Repa, A.H. Nguyen, A. Mehta, E.B. Webb III, L. A. Fredin, N.C. Strandwitz, Atomic-layer-deposited aluminum oxide thin films probed with X-ray scattering and compared to molecular dynamics and density functional theory models, ACS Omega 7 (2022) 41033–41043, <https://doi.org/10.1021/acsomega.2c04402>.
- [33] P. Lamparter, R. Kniep, Structure of amorphous Al₂O₃, Physica B 234–236 (1997) 405–406, [https://doi.org/10.1016/S0921-4526\(96\)01044-7](https://doi.org/10.1016/S0921-4526(96)01044-7).
- [34] C. Guerra-Núñez, M. Döbeli, J. Michler, I. Utke, Reaction and growth mechanisms in Al₂O₃ deposited via atomic layer deposition: elucidating the hydrogen source,

- Chem. Mater. 29 (2017) 8690–8703, <https://doi.org/10.1021/acs.chemmater.7b02759>.
- [35] S.R. Elliott, Medium-range structural order in covalent amorphous solids, Nature 354 (1991) 445–452, <https://doi.org/10.1038/354445a0>.
- [36] K. Xue, L.-S. Niu, H.-J. Shi, Effects of quench rates on the short- and medium-range orders of amorphous silicon carbide: a molecular-dynamics study, J. Appl. Phys. 104 (2008) 053518, <https://doi.org/10.1063/1.2974095>.
- [37] S.K. Lee, S.B. Lee, S.Y. Park, Y.S. Yi, C.W. Ahn, Structure of amorphous aluminum oxide, Phys. Rev. Lett. 103 (2009) 095501, <https://doi.org/10.1103/PhysRevLett.103.095501>.
- [38] R. Lizárraga, E. Holmström, S.C. Parker, C. Arrouvel, Structural characterization of amorphous alumina and its polymorphs from first-principles XPS and NMR calculations, Phys. Rev. B 83 (2011) 094201, <https://doi.org/10.1103/PhysRevB.83.094201>.
- [39] R. Hidayat, H.-L. Kim, Y.R. Sriwijaya, K. Khumaini, W.-J. Lee, Chemisorption of tetrakis(dimethylamino)zirconium on zirconium oxide: density functional theory study, Surf. Interfaces 50 (2024) 104480, <https://doi.org/10.1016/j.surfin.2024.104480>.
- [40] R.A. Wind, S.M. George, Quartz crystal microbalance studies of Al₂O₃ atomic layer deposition using trimethylaluminum and water at 125°C, J. Phys. Chem. A 114 (2010) 1281–1289, <https://doi.org/10.1021/jp9049268>.
- [41] A.C. Dillon, A.W. Ott, J.D. Way, S.M. George, Surface chemistry of Al₂O₃ deposition using Al(CH₃)₃ and H₂O in a binary reaction sequence, Surf. Sci. 322 (1995) 230–242, [https://doi.org/10.1016/0039-6028\(95\)90033-0](https://doi.org/10.1016/0039-6028(95)90033-0).
- [42] R. Hidayat, H.-L. Kim, K. Khumaini, T. Chowdhury, T.R. Mayangsari, B. Cho, S. Park, W.-J. Lee, Selective etching mechanism of silicon oxide against silicon by hydrogen fluoride: a density functional theory study, Phys. Chem. Chem. Phys. 25 (2023) 3890–3899, <https://doi.org/10.1039/D2CP05456F>.
- [43] A.M. Cano, A.E. Marquardt, J.W. DuMont, S.M. George, Effect of HF pressure on thermal Al₂O₃ atomic layer etch rates and Al₂O₃ fluorination, J. Phys. Chem. C 123 (2019) 10346–10355, <https://doi.org/10.1021/acs.jpcc.9b00124>.
- [44] J.W. DuMont, S.M. George, Competition between Al₂O₃ atomic layer etching and AlF₃ atomic layer deposition using sequential exposures of trimethylaluminum and hydrogen fluoride, J. Chem. Phys. 146 (2017) 052819, <https://doi.org/10.1063/1.4973310>.
- [45] J.-O. Carlsson, S. Gorbatkin, D. Lubben, J.E. Greene, Thermodynamics of the homogeneous and heterogeneous decomposition of trimethylaluminum, monomethylaluminum, and dimethylaluminumhydride: effects of scavengers and ultraviolet-laser photolysis, J. Vac. Sci. Technol. B 9 (1991) 2759–2770, <https://doi.org/10.1116/1.585642>.